Exploring the amplied role of HCHO in the formation of HMS and O₃ during the ~~wintertime~~co-occurring PM₂.₅ ~~ozone~~ and O₃ ~~PM₂.₅~~ pollution in a coastal city of southeast China

Youwei Hong[a,b,c,d,g]*, Keran Zhang[a,b,d], Dan Liao[f], Gaojie Chen[a,b,c], Min Zhao[i], Yiling Lin[a,b,e], Xiaoting Ji[a,b,c], Ke Xu[a,b,g], Yu Wu[a,b,e], Ruilian Yu[e], Gongren Hu[e], Sung-Deuk Choi[h], Likun Xue[i*], Jinsheng Chen[a,b,c]

[a]Center for Excellence in Regional Atmospheric Environment, Key Lab of Urban Environment and Health, Institute of Urban Environment, Chinese Academy of Sciences, Xiamen, 361021, China

[b]Fujian Key Laboratory of Atmospheric Ozone Pollution Prevention, Institute of Urban Environment, Chinese Academy of Sciences, Xiamen, 361021, China

[c]University of Chinese Academy of Sciences, Beijing, 100049, China

[d]College of Resources and Environment, Fujian Agriculture and Forest University, Fuzhou 350002, China

[e]College of Chemical Engineering, Huaqiao University, Xiamen, 361021, China

[f]College of Environment and Public Health, Xiamen Huaxia University, Xiamen 361024, China

[g]School of Life Sciences, Hebei University, Baoding, 071000, China

[h]Department of Urban and Environmental Engineering, Ulsan National Institute of Science and Technology, Ulsan, 44919, South Korea

[i]Environment Research Institute, Shandong University, Qingdao, 266237, China

*Corresponding author E-mail: Youwei Hong (ywhong@iue.ac.cn); Likun Xue (xuelikun@sdu.edu.cn)

Abstract:

To develop the effective strategies for controlling both $PM_{2.5}$ and O_3 levels, it is crucial to understand their synergistic mechanisms, key precursors, and atmospheric physiochemical processes involved. In this study, a wintertime co-occurring O_3 and $PM_{2.5}$ pollution event in a coastal city in southeast China was investigated based on high-time resolution measurements of criteria air pollutants, chemical compositions of $PM_{2.5}$, and O_3 precursors, such as NOx, HCHO, and VOCs. The results of this study revealed ~~the~~, characteristics, of ~~a~~ positive~~ly~~ ~~correlation~~ correlated ~~between~~ $PM_{2.5}$ and MDA8 O_3 concentrations ~~during the whole periods~~, ~~suggesting~~and ~~–~~an increase in atmospheric oxidation capacity (AOC) during the cold seasons. Strong correlations (R^2 = 0.415–0.477) ~~were observed~~ between HCHO, Fe, Mn, and sulfate concentrations were observed, suggesting the influence of catalyzed oxidation processes in the coastal city. Through an observation-based model (OBM) analysis coupled with the regional atmospheric chemistry mechanism version 2 (RACM2) and the chemical aqueous-phase radical mechanism version 3.0 (CAPRAM 3.0), we found that high concentrations of precursors (SO_2 and HCHO), high relative humidity, and moderately acidic pH conditions enhanced the heterogeneous formation of hydroxymethanesulfonate (HMS) in $PM_{2.5}$. Furthermore, by employing the Master Chemical Mechanism (OBM-MCM), we verified that disabling the HCHO mechanism could decrease daytime net O_3 production rates by reducing the production rates of

HO$_2$+NO. These results were consistent with the daily values of AOC, OH, HO$_2$, and RO$_2$ concentrations. This study contributes to a better understanding of the significance of HCHO in photochemical reactions and the formation of ~~secondary aerosols~~HMS in ~~a~~ coastal city.

Key words: PM$_{2.5}$; O$_3$; formaldehyde; OBM; coastal city

Introduction

Air pollution, dominated by fine particulate matter (PM$_{2.5}$) and ground-level ozone (O$_3$), is an important global environmental issue linked to climate change and human health, including cardiovascular and respiratory illnesses and mortality (Xiao et al., 2022; Vohra et al., 2022). To decrease global air pollution and associated mortality, the World Health Organization recently updated its air quality guideline for annual PM$_{2.5}$ exposure from 10 to 5 μg m^{-3} and added the average O$_3$ concentrations of no more than 60 μg m^{-3} during the peak season (WHO, 2021). To develop two-pollutant control strategies to decrease both PM$_{2.5}$ and O$_3$, there is a need to understand the synergistic mechanisms and spatiotemporal delineation between them (Ivatt et al., 2022; Li et al., 2019b).

There are complex synergistic effects between PM$_{2.5}$ and O$_3$, due to common precursors (e.g., NOx and VOCs), atmospheric physiochemical processes, and weather systems (Li et al., 2019a; Shao et al., 2022; Jia et al., 2023; Zhang et al., 2022; Qin et al., 2021; Qu et al., 2023). ~~Some studies have reported that O$_3$ could enhance the~~

带格式的: 字体颜色: 红色

71 ~~formation of secondary PM$_{2.5}$ by strengthening atmospheric oxidation capacity (Qin et~~

72 ~~al., 2022; Zhao et al., 2020).~~ An increase in O$_3$ concentration will increase oxidizing

73 substances, such as OH, H$_2$O$_2$, and RCHO, which promote the oxidation of SO$_2$, NOx,

74 and VOCs to secondary inorganic and organic components in PM$_{2.5}$ (Feng et al., 2020;

75 Lu et al., 2019). On the contrary, ~~PM$_{2.5}$ could affect O$_3$ formation by interfering with~~

76 ~~the radiation intensity of the Earth, providing a multiphase reaction surface and~~

77 ~~affecting the radiation flux and intensity of the boundary layer (Shao et al., 2021; Li et~~

78 ~~al., 2017). In addition,~~ multiphase reactions occur on the surface of atmospheric

79 particles, such as the ~~hydrolysis~~ uptake of ~~N$_2$O$_5$~~ HCHO and HO$_2$ absorption, thus

80 affecting the formation of O$_3$ ~~precursors NO$_2$~~ (Song et al., 2022; Lou et al., 2014).

81   Formaldehyde (HCHO) plays an important role in the photochemical reaction

82 process and secondary aerosol formation (Kalashnikov et al., 2022; Ma et al., 2020;

83 Song et al., 2021; Zong et al., 2021). Most studies have focused on pollution

84 characteristics and sources, particle uptake of HCHO, and their impacts on atmospheric

85 oxidation capacity (Liu et al., 2022b; Wu et al., 2023; Zhang et al., 2021). Recent

86 studies have shown that HCHO can react with hydrogen peroxide (H$_2$O$_2$) to produce

87 hydroxymethyl hydroperoxide (HMHP), which rapidly oxidizes dissolved sulfur

88 dioxide (SO$_2$, aq) to sulfate (Dovrou et al., 2022). Meanwhile, HCHO reacts with

89 dissolved SO$_2$ (aq) to produce hydroxymethanesulfonate (HMS, HOCH2SO−), which,

90 upon oxidation with the hydroxyl radical (OH), forms sulfate (Ma et al., 2020; Moch et

91 al., 2018, 2020). Totally,~~Recent studies have reported that~~ atmospheric HCHO

92 contributes to sulfate formation in PM$_{2.5}$ by producing HO$_2$ radicals and ~~hydroxymethyl~~

带格式的：字体颜色：自动设置

93 hydroperoxide (HMHP) ~~)~~ _or ~~hydroxymethanesulfonate~~ (HMS~~)~~ (Wu et al., 2023;

94 Dovrou et al., 2022; Campbell et al., 2022). However, ~~T~~these studies highlight the

95 necessity for more observation research to obtain evidence of the contributions of

96 HCHO to HMS formation. HMS is an important organosulfur compound in the

97 atmosphere, not only in cloud and fog but also in atmospheric aerosols (Munger et al.,

98 1986; Dixon and Aasen, 1999). The misidentification of HMS as inorganic sulfate

99 caused the overestimation of the observed particulate sulfate (Ma et al., 2020; Dovrou

100 et al., 2022). However, in subtropical coastal regions with apparent HCHO production,

101 further studies are required to investigate the impacts of HCHO on the the formations

102 of HMS and ROx radicals~~synergistic effects between PM2.5 and O3~~.

103   Xiamen, a coastal city in southeast China, has frequently experienced $PM_{2.5}$

104 pollution (with low O_3 concentrations) in winter and O_3 pollution in spring and autumn

105 (Hong et al., 2022; Wu et al., 2019). Our previous studies mainly focused on the

106 pollution characteristics of $PM_{2.5}$ or O_3 in different seasons and their sources associated

107 with anthropogenic emissions and the East Asian monsoon (Liu et al., 2020; Liu et al.,

108 2022a; Hong et al., 2021). At the end of winter and the beginning of spring in 2022, an

109 outbreak of co-occurring O_3 and $PM_{2.5}$ pollution was observed in Xiamen. Therefore,

110 it provided a unique opportunity to study the impacts of HCHO on the formations of

111 HMS and ROx radicals~~interactions among precursors, heterogeneous chemistry, and~~

112 ~~photochemical reactions for the~~ synergistic effects of $PM_{2.5}$ and O_3. In the coastal region,

113 there is an apparent alternation of polluted and clean air masses from continental and

114 ocean areas and a local geographical environment, including relatively high humidity,

115 dense vegetation, and strong atmospheric oxidation capacity (Hu et al., 2022; Wu et al.,

116 2020). Potential ~~synergistic mechanisms~~ roles and mechanisms of HCHO in the

117 photochemical reaction process and HMS formation ~~between O_3 and $PM_{2.5}$~~ would differ

118 from those in megacities of China, such as the Beijing-Tianjin-Hebei (BTH) Area, the

119 Yangtze River Delta (YRD), and the Pearl River Delta (PRD). Based on the

120 observation-based model (OBM) analysis, the objectives of this study are to (1)

121 characterize the wintertime co-occurring O_3 and $PM_{2.5}$ pollution process in a coastal

122 city; (2) elaborate the influence of HCHO on the heterogeneous formation of

123 ~~hydroxymethanesulfonate (~~HMS~~)~~ in $PM_{2.5}$; (3) explore the mechanisms of HCHO on

124 O_3 pollution and photochemical reactions process.

125

2 Methods and materials

2.1 Study area

128   The monitoring site (Institute of Urban Environment, Chinese Academy of

129 Sciences, 118.06° E, 24.61° N) is located in Xiamen, a coastal city in southeast China

130 (Fig. S1). It is situated in a subtropical monsoon climate, with an ~~annual~~ average

131 temperature of ~~23.3~~18.5°C and a relative humidity of ~~77.6~~63.3% during the wintertime

132 observation. In autumn and winter, cold and dry air masses move northward from inland,

133 while in late spring and summer, the prevailing air masses are southerly, characterized

134 by warm air temperatures and high humidity. The air-monitoring supersite is located on

135 the rooftop of a building, surrounded by residential buildings, educational institutions,

136 a commercial zone, and freeways. The downtown area of Xiamen, with a high

137 population density and frequent traffic jams, is located south of the monitoring site.

138

139 **2.2 Observation**

140   Gas and aerosol species, O_3 precursors, photolysis rate, and meteorological

141 parameters were continuously measured online from February 17 to March 17, 2022.

142 Hourly mass concentrations of $PM_{2.5}$ and PM_{10} were measured using a tapered element

143 oscillating microbalance (TEOM1405, Thermo Scientific Corp., MA, USA). NO/NO_2,

144 SO_2, and O_3 were monitored using continuous gas analyzers (TEI 42i, 43i, and 49i,

145 Thermo Scientific Corp., MA, USA). HCHO analyzer (FMS-100, Focused Photonics

146 Inc., Hangzhou, China) was used to measure gaseous HCHO based on the Hantzsch

147 reaction, according to our previous method (Liu et al., 2022b). Water-soluble inorganic

148 ions (WSII) in $PM_{2.5}$ (Cl^-, SO_4^{2-}, NO_3^-, Na^+, K^+, NH_4^+, Mg^{2+}, and Ca^{2+}) were measured

149 hourly using a Monitoring device for AeRosols and Gases in ambient Air (MARGA

150 2080; Metrohm Applikon B.V.; Delft, Netherlands). Simultaneously, organic carbon

151 (OC) and elemental carbon (EC) in $PM_{2.5}$ were measured using an OC/EC analyzer

152 (model RT-4; Sunset Laboratory Inc.; Tigard, USA). BC was monitored using an

153 Aethalometer (AE31, Magee Scientific, USA) with a $PM_{2.5}$ cut-off inlet. Besides,

154 concentrations of 22 elements (Al, Si, S, Fe, K, Mn, Pb, Ca, Zn, Ba, V, Cu, Ni, As, Cr,

155 Ag, Se, Br, Hg, Sn, Ti, and Sb) were measured using a multi-metal monitor (Xact™

156 625, Cooper Environmental Services, LLT; Portland, USA). Strict quality assurance

157 and quality control procedures were applied, and the maintenance and accuracy of all

158 online instruments were validated (Hong et al., 2021). The detection limits, time

159 resolutions and measured uncertainties of air pollutants were shown in TableS3.

160   A gas chromatograph-mass spectrometer (GC-FID/MS, TH-300B, Wuhan, China)

161 was used to measure ambient VOCs with one-hour time resolution, following the

162 method from our previous studies (Liu et al., 2020a,b). Briefly, the air sample was

163 preconcentrated by cooling to −160 °C in a cryogenic trap, then heated to 100 °C, and

164 subsequently transferred to the secondary trap using high-purity helium (He). The low-

165 carbon (C2-C5) hydrocarbons were detected using a flame ionization detector (FID)

166 with a PLOT (Al_2O_3/KCl) column (15 m × 0.32 mm × 6.0 μm), while other VOC

167 species were quantified using a GC/MS with a DB-624 column (60 m × 0.25 mm × 1.4

168 μm). The instrument can quantify 106 VOC species, including 29 alkanes, 11 alkenes,

169 one alkyne, 17 aromatics, 35 halogenated hydrocarbons, and 13 OVOCs. Calibration

170 was performed daily at 2311:00 pm using the standard mixtures of US EPA PAMS and

171 TO-15. The detection limits of the measured VOCs ranged from 0.02 ppbv to 0.30 ppbv.

172   Ambient meteorological parameters, including relative humidity (RH),

173 temperature (T), wind speed (WS), and wind direction (WD), were obtained using an

174 ultrasonic atmospherium (150WX, Airmar, USA). Photolysis frequencies and HCHO

175 were measured using a photolysis spectrometer PFS-100 and a formaldehyde monitor

176 FMS-100 (Focused Photonics Inc., Hangzhou, China), respectively. The photolysis rate

177 constants include $J(O^1D)$, $J(NO_2)$, $J(H_2O_2)$, $J(HONO)$, $J(HCHO)$, and $J(NO_3)$. The

178 distribution of fire spots during the observation periods was obtained from the Fire

179 Information   for   Resource   Management   System

180 (https://firms.modaps.eosdis.nasa.gov/firemap/). The data for boundary layer height

181 (BLH) were obtained from the European Centre for Medium-Range Weather Forecasts

182 (ECMWF)   ERA5   hourly   reanalysis   dataset

183 (https://www.ecmwf.int/en/forecasts/datasets/reanalysis-datasets/era5, last access:

184 March 24, 2023). The resolution of ERA-5 reanalysis is 0.25°×0.25°.

185

186 **2.3 Positive matrix factorization (PMF) analysis**

187   The PMF 5.0 model was applied to quantify high-time-resolution sources of $PM_{2.5}$

188 during the observation periods. The details of the model analysis were described in our

189 previous studies (Hong et al., 2021; Liu et al., 2020). Briefly, Eq. (1) demonstrates j

190 compound species in the ith sample as the concentration from p independent sources.

$$x_{ij} = \sum_{k=1}^{p} g_{ik} f_{ki} + e_{ij}$$

191   (1)

192   Where e_{ij} is the residual for each species, f_{kj} is the fraction of the jth species from

193 the kth source, g_{ik} is the species contribution of the kth source to the ith sample, x_{ij} is

194 the jth species concentration measured in the ith sample, and p is the total number of

195 independent sources. The Q value (Eq. (2)), based on the uncertainties (μ), was used to

196 evaluate the steadiness of the solution.

$$Q = \sum_{i=1}^{n} \sum_{j=1}^{m} \left[\frac{x_{ij} - \sum_{k=1}^{p} g_{ik} f_{kj}}{\mu_{ij}} \right]^2$$

197   (2)

198

199 **2.4 Observation-based model (OBM)**

The OBM-MCM model is employed to simulate in situ atmospheric photochemical processes and quantify the O_3 production rate, AOC, and OH reactivity. The details of the OBM-MCM model were reported in our previous studies (Liu et al., 2022a,b). In summary, monitoring data with a one-hour time resolution of air pollutants (i.e., O_3, CO, NO, NO_2, HONO, SO_2, and VOCs), meteorological parameters (i.e., T, P, and RH), and photolysis rate constants ($J(O^1D)$, $J(NO_2)$, $J(H_2O_2)$, $J(HONO)$, $J(HCHO)$, and $J(NO_3)$) were input into the OBM-MCM model as constraints for the model simulation. The photolysis rates of other molecules were determined by solar zenith angle and scaled using measured JNO_2 values (Saunders et al., 2003). According to our previous studies, Tthe model incorporates the physical process of deposition within the boundary layer height (BLH), which varies from 300 m during nighttime to 1500 m during the daytime in ~~autumn~~ winter (Li et al., 2018;Liu et al., 2022). Therefore, dry deposition velocities were used to simulate the deposition loss of certain reactants in the atmosphere (Zhang et al., 2003; Xue et al., 2014).

To simulate the concentration of particulate HCHO and its role in the heterogeneous formation of hydroxymethanesulfonate (HMS), the observation-based zero dimensional multiphase chemical box model was used, of which the gas phase chemistry is described by he regional atmospheric chemistry mechanism version 2 (RACM2) and the aqueous phase part of the mechanism is represented by the chemical aqueous-phase radical mechanism version 3.0 (CAPRAM 3.0). The mass transfer processes between the gas and aqueous phases is also considered in current model according to Schwartz (1986). The Henry's law constant of HCHO was updated with a

value of 0.31×10^8 M atm^{-1}, as estimated by Mitsuishi et al. (2018). Sensitivity analysis

was conducted to evaluate the uncertainties introduced by the Henry's law constant,

details can be found in SI. For major production and loss paths of HMS, dissolved

HCHO reacts with sulfite and bisulfite to form HMS (Eq (3-4)), which can be further

oxidized by aqueous OH radicals (Eq (5)), details about the HMS mechanisms and the

corresponding reaction kinetics are documented in CAPRAM website

(https://capram.tropos.de/). ~~To simulate the concentration of particulate HCHO and its~~

~~role in the heterogeneous formation of hydroxymethanesulfonate (HMS), we combined~~

~~the OBM model with the regional atmospheric chemistry mechanism version 2~~

~~(RACM2) and the chemical aqueous phase radical mechanism version 3.0 (CAPRAM~~

~~3.0). We also considered the mass transfer processes between the gas and aqueous~~

~~phases (Schwartz, 1986). The Henry's law constant of HCHO is 0.31×10^8 M atm^{-1}, as~~

~~estimated by Mitsuishi et al. (2018). For the aqueous HMS formation mechanisms,~~

~~dissolved HCHO reacts with sulfite and bisulfite to form HMS (Eq (3-4)), which can~~

~~be further oxidized by aqueous OH radicals (Eq (5)).~~

$$HCHO_{(aq)} + HSO_3^- = HOCH_2SO_3^- \tag{3}$$

$$HCHO_{(aq)} + SO_3^{2-} + H_2O = HOCH_2SO_3^- + OH^- \tag{4}$$

$$HOCH_2SO_3^- + OH\cdot = 2SO_4^{2-} + HCHO_{(aq)} + 3H^+ \tag{5}$$
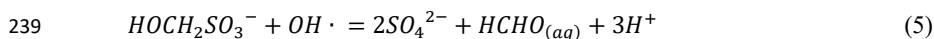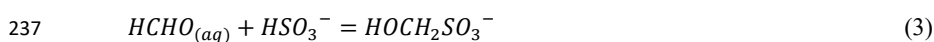
For detailed modeling steps of HMS, firstly, the observation data of gaseous NO,

NO$_2$, O$_3$, SO$_2$, CO, NMHCs, HCHO and other ten carbonyls, particulate phase NO$_3^-$,

NH$_4^+$, and Cl$^-$, along with meteorological parameters were averaged or interpolated into

243 a 1-h time resolution and classified into model recognized groups as model inputs,

244 while the measured SO_4^{2-} was used as the initial conditions. Liquid water content (LWC)

245 and aqueous H^+ concentrations, calculated using the ISORROPIA-II model (Hong et

246 al., 2022), were also used as model inputs. Then, model calculations were conducted

247 using the commercial FACSIMILE software, the modeling period was from February

248 26 to March 16, 2022 and each day was regarded as an independent simulation case.

249 The model was constrained every hour by the input observation data for integral

250 calculation. For each case, The integration ran three times in series to steady the

251 unconstrained species (e.g., radicals), which was initiated at 00:00 local time (LT), and

252 had a step of 1 h and a duration of 24 h. Finally, the modeled HMS concentrations of

253 the third run were outputted with a 1-hour time resolution for further analysis. The

254 observation data of gaseous NO, NO₂, O₃, SO₂, CO, HCHO, VOCs, particulate phase

255 NO₃⁻, NH₄⁺, and Cl⁻, along with meteorological parameters with a 1-h time resolution

256 were interpolated to constrain the model, while the measured SO₄²⁻ was used as the

257 initial condition for the model simulation. Liquid water content (LWC) and aqueous H⁺

258 concentrations, calculated using the ISORROPIA-II model (Hong et al., 2022), were

259 also used to constrain the model. Model calculations were conducted from February 26

260 to March 16, 2022. For each case, the model was initiated at 00:00 local time (LT), and

261 the integration had a step of 1 h and a duration of 24 h.

262

263 **2.5 Backward trajectory analysis**

264 Hybrid Single-Particle Lagrangian Integrated Trajectory (HYSPLIT) was used to

3 Results and discussions

3.1 Overview of co-occurring O_3 and $PM_{2.5}$ pollution

The time series of criteria air pollutants, O_3 precursors, and meteorological parameters from February 17 to March 17, 2022 are shown in Fig. 1. Two typical $PM_{2.5}$ and O_3 pollution episodes (EP1: February 26 to March 5; EP2: March 11 to March 17) were observed, compared to the other periods (Pre-EP1: February 11 to February 25 and Pre-EP2: March 16 to March 10) affected by rainfall. The mean concentrations of $PM_{2.5}$ during EP1 and EP2 were 51.9 μg m^{-3} and 35.3 μg m^{-3}, respectively, compared to 9.03 μg m^{-3} during Pre-EP1 (Table S1). The concentrations of other air pollutants, such as O_3, SO_2, NO_2, PM_{10}, OC, EC, BC, HCHO, and VOCs, showed a significant increasing trend during EP1 and EP2. During the monitoring periods, the concentrations of measured HCHO ranged from 0.68 ppbv and 3.59 ppbv (Tabe S1). According to our previous studies (Liu et al., 2023), the average levels of the measured HCHO in spring and autumn in Xiamen were 2.9 ± 0.3 ppbv and 3.2 ± 1.4 ppbv, respectively. Totally, the HCHO level in Xiamen was lower than that in megacities (Table S2), such as Beijing (summer: 11.39±5.58 ppbv), Hongkong (summer:

286 8.07±1.94 ppbv), and Guangzhou (summer: 6.69±1.98 ppbv), while was comparable to

287 the coastal cities, including Shenzhen (spring: 3.4±1.6 ppbv), Yantai (summer:

288 3.90±1.12 ppbv), and Shanghai (summer:3.31±1.43 ppbv). In the coastal cities of

289 southeastern China, halogenated VOC is one of important VOC species, which

290 originated from industrial emissions and solvent usage (Chen et al., 2022; Ji et al., 2022;

291 Liu et al., 2022). In this study, during the monitoring period, backward trajectories

292 showed air mass transport from the northeast, which brought halogenated VOC from

293 Quanzhou city, an industrial city adjacent to Xiamen.

294 The maximum $PM_{2.5}$ and O_3 concentrations were approximately 100 μg m^{-3} and

295 200 μg m^{-3}, respectively. The maximum daily 8 h average (MDA8) O_3 concentrations

296 were calculated according to the Ambient Air Quality Standard of China. Fig. S2 shows

297 the positive correlation between $PM_{2.5}$ and MDA8 O_3 concentrations during the whole

298 period. In Xiamen, a coastal city in Southeast China, the annual mean concentrations

299 of criteria air pollutants from 2015 to 2021 were significantly lower than in other

300 Chinese cities (Fig. S3) (Li et al., 2022; Shao et al., 2022). Meanwhile, inter-annual

301 averaged concentrations of O_3 and Ox in winter were shown in Fig S3, suggesting an

302 increase in atmospheric oxidation capacity (AOC) during the cold seasons. Therefore,

303 these two typical $PM_{2.5}$ and O_3 pollution episodes (EP1 and EP2) might beare worth

304 exploring in terms of the formation mechanisms and synergistic effects of $PM_{2.5}$ and O_3

305 in the coastal city.

306
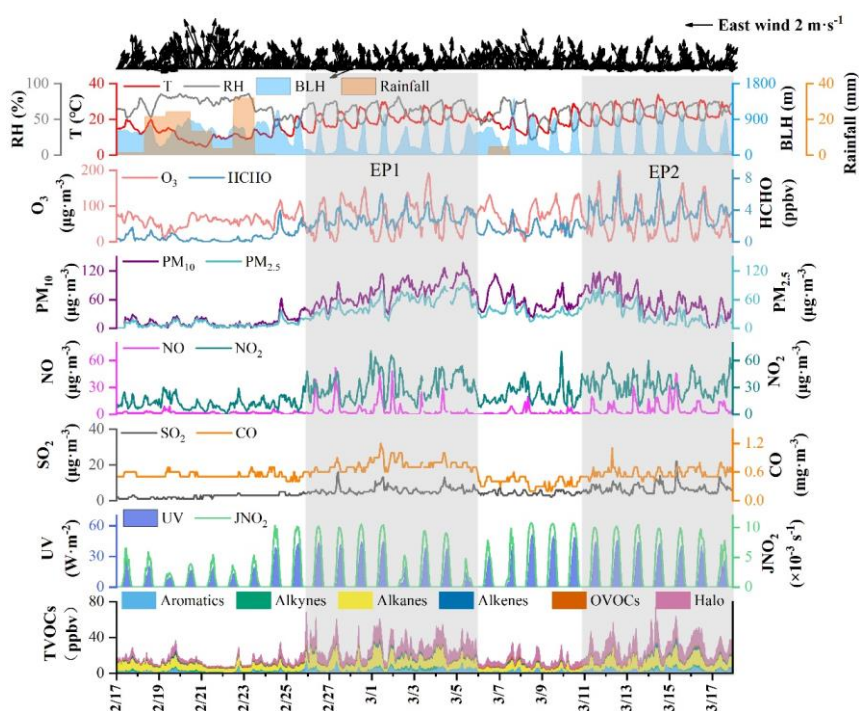
Fig. 1. Time series of various air pollutants and meteorological parameters

308

3.2 Chemical compositions and sources of PM₂.₅

As shown in Figure 2, an overall increasing trend is clearly observed in both bulk PM₂.₅ and its major components during EP1 and EP2. Nitrate and organic matter (OM) remain the top two dominant PM₂.₅ components, followed by sulfate and ammonium. The mean concentrations of SO_4^{2-}, NO_3^-, and NH_4^+ during EP1 and EP2 were 7.07 μg m⁻³ and 5.87 μg m⁻³, 14.95 μg m⁻³ and 9.69 μg m⁻³, and 6.77 μg m⁻³ and 4.46 μg m⁻³, respectively (Table S1). The increase in EC indicates the contributions of local anthropogenic emission sources, such as vehicle exhausts (Fig. 2). The concentrations

and percentages of OC and EC during different periods are illustrated in Fig. S4 and

Table S1. The average OC and EC concentrations during EP1 and EP2 were 6.36 μg

m^{-3} and 7.48 μg m^{-3} and 1.23 μg m^{-3} and 1.29 μg m^{-3}, respectively, which were notably

higher than those during Pre-EP1 and Pre-EP2. These results are consistent with the

increase in primary emissions and secondary formation contributing to complex air

pollution during the rapid urbanization and industrialization stages in China (Xiao et

al., 2022; Jiang et al., 2022).
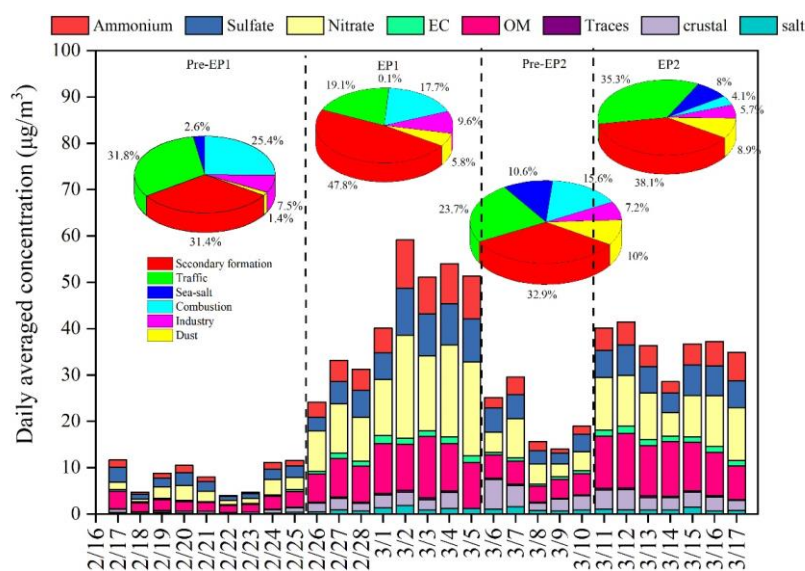
Fig. 2. Time series of PM$_{2.5}$ chemical composition and sources apportionment by the PMF model. In the legends, OM refers to organic matter, calculated as 1.4×OC; "Tracers" includes elements other than Na, Cl, S, K, Al, Si, Ca, Fe; "Crustal" represents crustal materials, calculated as 1.89×Al+2.14×Si+1.4×Ca+1.43×Fe; and "Salts" includes Na$^+$ and Cl$^-$.

The PMF model was applied to conduct high-time-resolution source

apportionment of PM$_{2.5}$, based on online hourly measurement data (Hong et al., 2021;

Chow et al., 2022). The factor profiles and the contributions of various sources to PM$_{2.5}$

332 are shown in Fig. 2 and Fig. S5. Previous studies have indicated that construction and

333 road dust is characterized by high loadings of Al, Si, Ca^{2+}, Na^+, Mg^{2+}, and Zn (Rienda

334 and Alves, 2021). In this study, the factor of dust (Factor 1) was identified by the high

335 contributions of Si (Fig. S5). The PMF analysis revealed that the contribution of dust

336 to $PM_{2.5}$ ranged from 5.8% to 8.9% during EP1 and EP2, compared to 1.4% during Pre-

337 EP1 (Fig.2). Factor 2, contributing to the high loading of metal elements (Mn, Zn, Fe,

338 Pb, and As), was characterized by industrial emissions (Belis et al., 2019). The

339 contributions from the industry during EP1 and EP2 remained constant. In factor 3, K^+

340 was dominant, and it was identified as coming from combustion sources (Watson et al.,

341 2001). Biomass burning could change the contribution of combustion to $PM_{2.5}$ at the

342 monitoring site through long-range transport. During EP2, the influence of combustion

343 sources (e.g., biomass burning) significantly decreased, due to reduced anthropogenic

344 emissions and the arrival of clean air masses from the ocean (Figs. S6 and S7). Factor

345 4, with the highest proportion of Na^+ and Mg^{2+} loadings, was associated with the

346 influence of sea-salt aerosol (Polissar et al., 1998). The percentages of sea salt (8-10%)

347 during Pre-EP2 and EP2 were relatively high. Factor 5 exhibited high contributions of

348 EC, OM, and Pb, which are general indicators of vehicle exhaust (Belis et al., 2019).

349 During EP2, the contribution of traffic increased up to 35.3%. Factor 6 was associated

350 with secondary aerosol, characterized by high loadings of SO_4^{2-}, NO_3^-, and NH_4^+. The

351 increased contributions of secondary formation during EP1 and EP2 accounted for 47.8%

352 and 38.1%, respectively.

353

3.3 Formation mechanism of PM$_{2.5}$

As shown in Fig. S8, SO$_4^{2-}$ was correlated with NH$_4^+$ (R^2 = 0.72–0.88), and the line fit of NH$_4^+$ and SO$_4^{2-}$ showed a slope of 1.78-2.67, suggesting the dominant form of (NH$_4$)$_2$SO$_4$. Similarly, NO$_3^-$ was also correlated with NH$_4^+$ (R^2 = 0.77–0.93), indicating the presence of NH$_4$NO$_3$. In addition, the ratio of NH$_4^+$ to the sum of NO$_3^-$ and SO$_4^{2-}$ was close to 1, indicating complete neutralization of sulfate and nitrate by ammonium (Fig. 8c). However, there was no significant difference in the existing form of SNA in PM$_{2.5}$ during EP1 and EP2~~under different periods~~.

The variations of sulfur oxidation rate (SOR) and nitrogen oxidation rate (NOR) under different periods are shown in Table S1. It should be noted that SOR (0.38±0.18) and NOR (0.32±0.08) during EP1 were the highest, indicating a high oxidation rate of SO$_2$ and NO$_2$. According to RH, T, and UV (Table S1), noticeable differences in meteorological conditions were observed under different periods. In this study, LWC was positively correlated with SO$_4^{2-}$, NO$_3^-$, and NH$_4^+$ (known as the secondary inorganic aerosol, SIA) (Fig. S9), suggesting the influence of the aqueous phase process, including reactions with O$_3$, OH, H$_2$O$_2$, and organic peroxides (Gen et al., 2019; Wang et al., 2023).

Current studies have found that O$_3$, H$_2$O$_2$, OH, and transition-metal-catalyzed (TMI) O$_2$ can trigger the secondary formation of SO$_4^{2-}$ (Hong et al., 2021; Gen et al., 2019). However, the relative importance of these oxidants in enhancing the formation of SO$_4^{2-}$ is still a topic of debate. As shown in Fig. 3(b) and (c), a good correlation was found between SO$_4^{2-}$ and Fe and Mn. The TMI-catalyzed oxidation contributed to the

376 formation of SO_4^{2-}, which occurred in both cloud processes and during haze episodes

377 (Li et al., 2020) because the Mn catalytic reaction rapidly occurred at the aerosol surface

378 and could oxidize S(IV) through the production of intermediate Mn(III) (Wang et al.,

379 2021). Even at very low concentrations of Mn, the Mn catalytic reaction, consuming

380 oxygen and SO_2, could produce sulfate. Under low aerosol pH conditions, the catalytic

381 reaction of TMIs plays an important role in the oxidation of S(IV). In this study, low

382 aerosol pH ranged from 2 to 4 was observed, indicating the potential influence of TMI-

383 catalyzed oxidation. In the future, it is vital to further evaluate the interaction of sulfate

384 formation and Fe/Mn, and to elucidate the main pathway of the S(IV) oxidation in the

385 coastal areas. In addition, as an important intermediate product in atmospheric

386 photochemical reactions, the formation and removal of HCHO are closely related to

387 OH and HO_2 radicals, which directly affect atmospheric reactivity and oxidation ability

388 (Wu et al., 2023; Zhang et al., 2021). In this study, the correlations ($R^2 = 0.415$) between

389 HCHO and sulfate concentrations were also examined, as displayed in Fig. 3(a). Recent

390 studies have shown that HCHO can react with hydrogen peroxide (H_2O_2) to produce

391 hydroxymethyl hydroperoxide, which rapidly oxidizes dissolved sulfur dioxide (SO_2,

392 aq) to sulfate (Dovrou et al., 2022). Meanwhile, HCHO reacts with dissolved SO_2 (aq)

393 to produce hydroxymethanesulfonate (HMS), which, upon oxidation with the hydroxyl

394 radical (OH), forms sulfate (Ma et al., 2020; Moch et al., 2020).

395
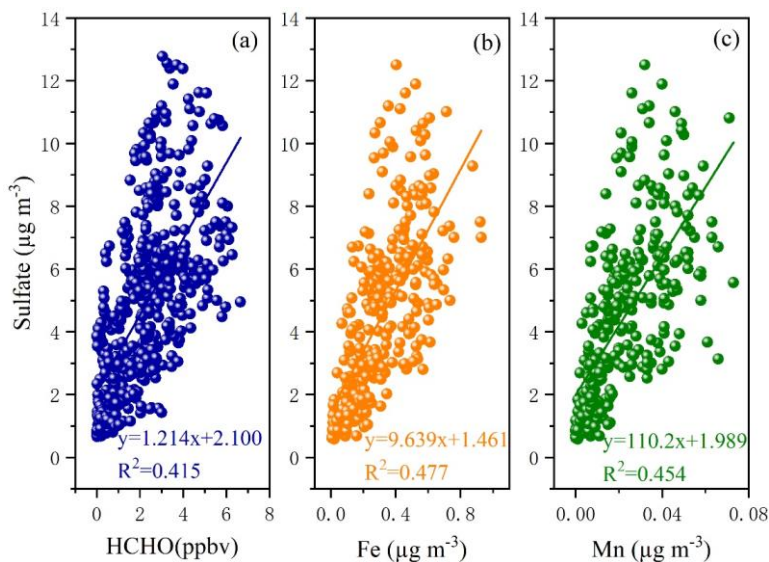
Fig.3. Correlations between the concentrations of sulfate and HCHO (a), Fe (b), and Mn (c)

397

3.4 Effects of HCHO on HMS in PM$_{2.5}$

To calculate the particulate concentrations of HC~~O~~HO and its contributions to the heterogeneous formation of HMS, we conducted the in-situ multiphase chemical simulations by combining the zero dimensional multiphase chemical box model with RACM2 and CAPRAM 3.0~~we combined the OBM model with RACM2 and CAPRAM 3.0~~. During EP1 and EP2, the concentrations of HCHO (aq) and HMS (aq), as well as the particulate sulfur molar percentage, increased with the rise of, SO$_2$, SO$_4^{2-}$, and HCHO concentrations (Fig. 4). Also, particulate sulfur molar percentage was higher during the pollution periods, which may due to the high concentrations of gaseous precursors (SO$_2$, HCHO) and favorable aerosol properties (i.e. pH and aerosol water

content) promoted the heterogeneous processes. Previous studies have modeled that 1 ppb of gas-phase HCHO could yield up to ~5 $\mu g \, m^{-3}$ HMS and identified that HCHO emissions was one of key factors controlling HMS formation during the winter haze (Moch et al., 2018). All above signify the important contributions of HCHO on the heterogeneous formation of HMS and particulate sulfur chemistry, especially during the pollution periods.

However, the molar ratio of HMS to sulfate were very low, suggesting the limited contributions of HMS concentrations to inorganic sulfate concentrations. Potential roles of HCHO in the HMS formation in coastal city of southeast China was differed from those in the megacities of China. ~~The increase in sulfate concentration was assocaited with the increase in LWC (Fig. S9). Previous studies indicated that the pH and liquid water content of aerosols were the main factors influencing the HCHO uptake coefficient (γ). Moreover, γ has a strong positive exponential relationship with aqueous sulfate concentration (Xu et al., 2022).~~ ~~Meanwhile,~~ Previous studies found that HCHO reacts with dissolved SO_2 (aq) to produce hydroxymethanesulfonate (HMS), which, upon oxidation with the hydroxyl radical (OH), forms sulfate (Ma et al., 2020; Moch et al., 2020). Ma et al. (2020) reported that heterogeneous formation of HMS accounted for 15% of OM, and resulted in 36% overestimates of sulfate during the winter haze in Beijing. ~~The increase in sulfate concentration was assocaited with the increase in LWC (Fig. S9). Previous studies indicated that the pH and liquid water content of aerosols were the main factors influencing the HCHO uptake coefficient (γ). Moreover, γ has a strong positive exponential relationship with aqueous sulfate concentration (Xu et al.,~~

430 ~~2022).~~

432
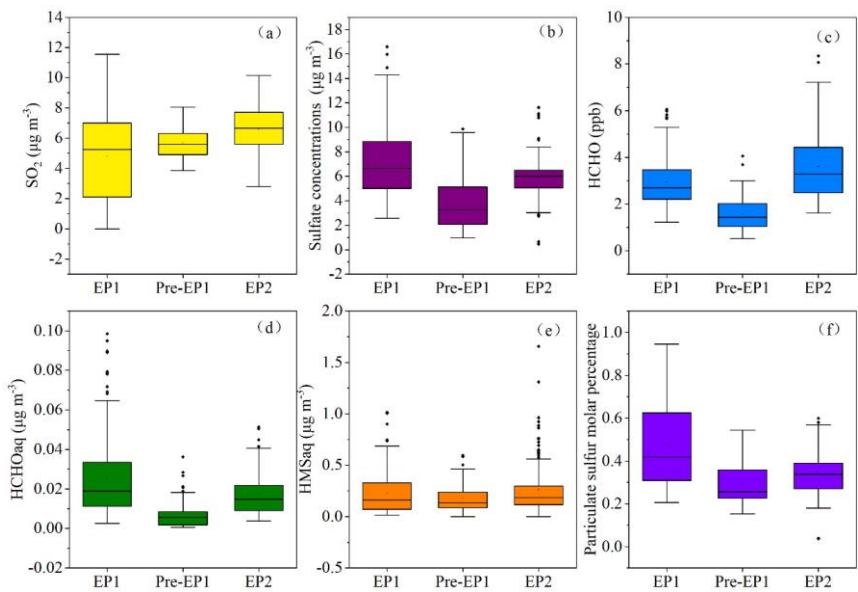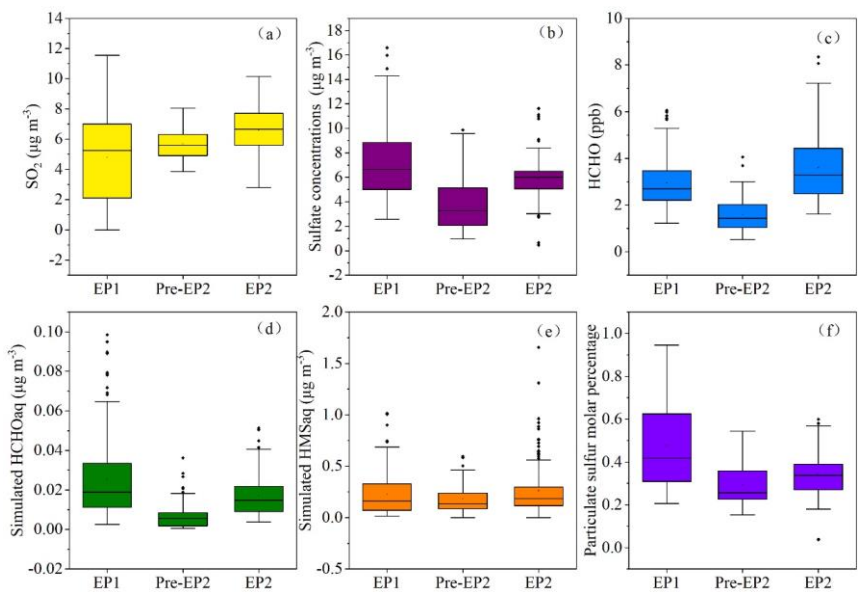
**Figure 4. Concentrations of SO₂, SO₄²⁻, and HCHO~~, HCHO (aq), HMS (aq), and particulate~~
~~sulfur molar percentage~~ observed at different pollution ~~levels~~stages.~~－~~ The simulated HCHO
(aq) and HMS (aq) were also presented. ~~In the box-whisker plots, the whiskers, boxes, and~~**

436 ~~points indicate the 5th/95th, 25th/75th, 50th percentiles, and mean values.~~ **The particulate**
437 **sulfur molar percentage was calculated as [n(SO$_4^{2-}$)+n(HMS)]/[n(SO$_4^{2-}$)+n(HMS)+ n(SO$_2$)].** In
438 the box–whisker plots, the whiskers, boxes, and points indicate the 5th/95th, 25th/75th, 50th
439 percentiles, and mean values.

440 ~~As shown in Fig. 5, the concentration of HMS exhibited a similar diurnal variation~~
441 ~~to that of HCHO (aq). These findings are consistent with the fact that HMS is formed~~
442 ~~throuhg the reaction between dissolved SO$_2$ and formaldehyde (HCHO) in aerosol~~
443 ~~liquid water. In our previous studies, we osbserved that gaseous HCHO showed an~~
444 ~~increasing trend after sunrise, peaking at noon due to photochemical reactions (Liu et~~
445 ~~al., 2022b). However, during EP1 and EP2, high concentrations of HCHO (aq) were~~
446 ~~observed during nighttime. Meanwhile, the heterogeneous formation of HMS also~~
447 ~~occurred, resulting in elevated HMS concentrations during nighttime.~~
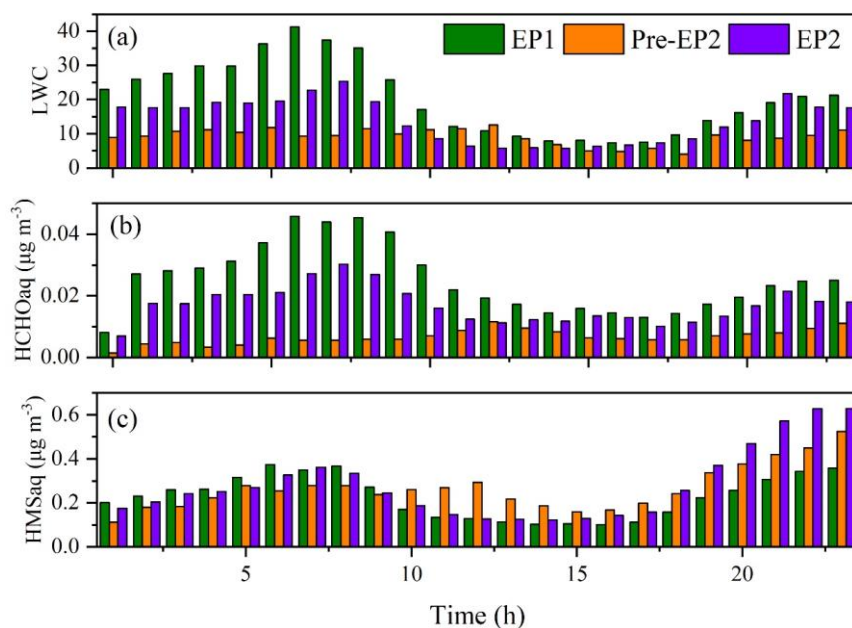
448
449 ~~**Figure 5. Diurnal variations of calculated HCHO (aq) and HMS (aq) at different pollution**~~
450 ~~**levels**~~

451   ~~In this study, h~~High concentrations of HMS were ~~observed~~ captured under high

452   RH and moderately acidic pH conditions (Fig. ~~6~~5). Previous studies have also indicated

453   that high RH promotes rapid HMS formation during winter haze, as the aerosol water

454   content could provide numerous reaction interfaces for HMS formation (Ma et al.,

455   2020). Meanwhile, atmospheric sulfur tended to distribute into the particle phase with

456   increasing RH. Fig. ~~6~~5 shows that HMS formation is favored under pH conditions close

457   to 4.0. Previous studies reported that high HMS concentrations were found under

458   moderate-pH conditions, as low pH inhibits HMS formation, and high pH is unsuitable

459   for its preservation (Ma et al., 2020; Campbell et al., 2022). Therefore, the combination

460   of high precursor concentrations (SO_2 and HCHO), high RH, and moderately acidic pH

461   enhanced the heterogeneous formation of HMS in ~~this~~ the coastal city.
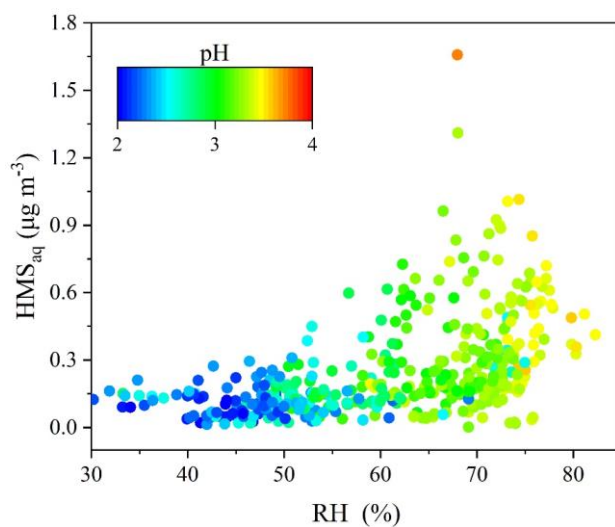
462

463   **Figure ~~6~~5. Evolution of HMS (aq) distribution with increasing RH, colored according to**
464   **aerosol pH.**

465

466   **3.5 Effects of HCHO on O_3 formation**

To investigate the effects of HCHO on O_3 formation during the co-occurring O_3 and $PM_{2.5}$ pollution period, the OBB was used to quantify the detailed O_3 production and loss pathways in both scenarios: input HCHO (IH) and non-input HCHO (NIH) (Fig. ~~7~~ 6 and Fig. ~~S10~~S9). The daytime production rates of HO_2+NO and RO_2+NO in the IH scenario were calculated to be 6.84 and 1.25 ppbv h^{-1} for EP1 and 9.91 and 2.17 ppbv h^{-1} for EP2, respectively. Meanwhile, the predominant O_3 loss reaction in this scenario was $OH+NO_2$, with rates of 2.26 ppbv h^{-1} for EP1 and 3.17 ppbv h^{-1} for EP2, followed by O_3 photolysis with rates of 0.77 ppbv h^{-1} and 1.10 ppbv h^{-1}. In contrast, the daytime production rates of HO_2+NO and RO_2+NO in the NIH scenario were 4.03 and 0.85 ppbv h^{-1} for EP1 and 4.86 and 1.29 ppbv h^{-1} for EP2, respectively. These results indicate that disabling the HCHO mechanism reduced the production rates of HO_2+NO by 41% for EP1 and 51% for EP2. In addition, the average maximum net O_3 production rate ~~observed~~ with the IH scenario was 5.02 ppb h^{-1} for EP1 and 7.93 ppb h^{-1} for EP2, approximately two times higher than the values of 2.48 ppb h^{-1} and 3.14 ppb h^{-1} ~~observed~~ with the NIH scenario. The results showed that the daytime net O_3 production rates decreased by 50–60% when the HCHO mechanism was disabled, probably due to the decrease in ROx concentrations and radical propagation rates (Wu et al., 2023; Zhang et al., 2021).

485
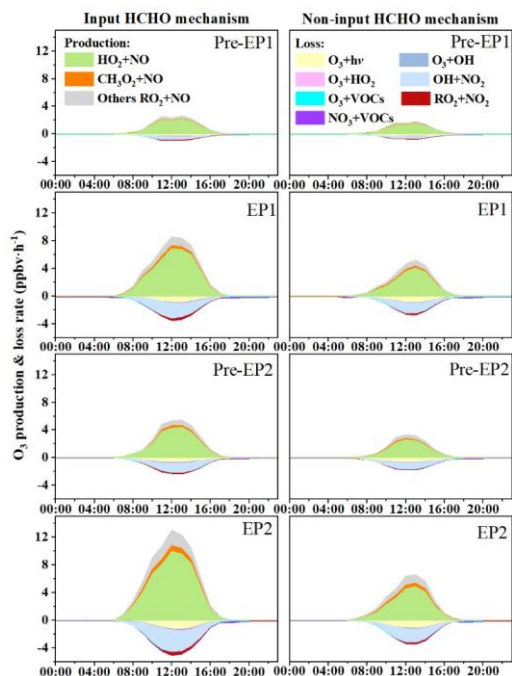
Figure 7~~6~~. O₃ production and loss rates by the OBM with and without the HCHO
mechanism

The atmospheric oxidation capacity (AOC) is a critical factor in determining the production rate of secondary pollutants and atmospheric photochemical pollution (Jia et al., 2023; Qin et al., 2022). In this study, AOC is calculated as the sum of the oxidation rates of various primary pollutants (e.g., CO, NOx, and VOCs) by major oxidants (i.e., OH, O_3, and NO_3). The model-simulated AOC, OH, HO_2, and RO_2 under different periods are shown in Fig. ~~8~~7 and Fig. ~~9~~8. The daily maximum AOC during EP1 and EP2 was 8.24×10^7 and 11.6×10^7 molecules cm^{-3} s^{-1}, respectively, which were higher than those (2.56×10^7 and 5.39×10^7 molecules cm^{-3} s^{-1}) in other periods. However, when the HCHO mechanism was disabled, the daily maximum AOC during different

497   stages decreased significantly. Especially, HCHO played much important role in AOC

498   during the co-occuring $PM_{2.5}$ and O_3 pollution periods. All these results are comparable

499   to rural sites in Hong Kong (6.2×10^7) and Berlin (1.4×10^7 molecules cm^{-3} s^{-1}) but

500   lower than those observed in highly polluted cities, such as Santiago (3.2×10^8

501   molecules cm^{-3} s^{-1}) and Shanghai (1.0×10^8 molecules cm^{-3} s^{-1}) (Li et al., 2018; Xue et

502   al., 2016; Liu et al., 2022a). These studies have reported that the variations in AOC are

503   related to precursor concentrations/types and photochemical conditions.

504
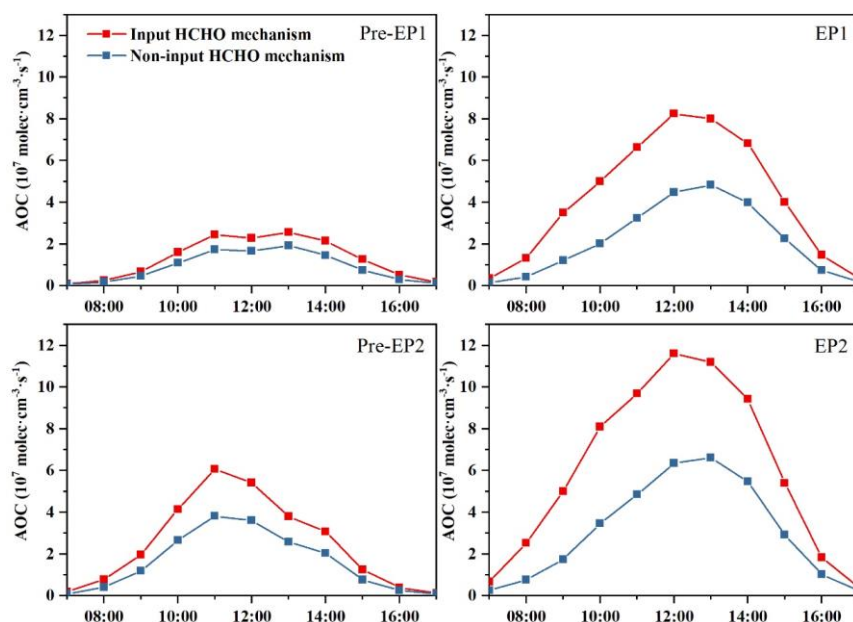
Figure 87. Atmospheric oxidation capacity (AOC) calculated by the OBM with and without the HCHO mechanism.

507   In addition, the maximum daily concentrations of OH, HO_2, and RO_2 exhibited a

508   similar pattern to that of AOC in both the IH and NIH scenarios (Fig. 98). Therefore,

509   the O_3 production rate during EP1 and EP2 was consistent with the maximum daily

510   values of AOC, OH, HO$_2$, and RO$_2$. The differences in ROx levels between the IH and

511   NIH model scenarios were also calculated (Fig. ~~S11~~S10). In this study, disabling the

512   HCHO mechanism led to decreased ROx concentrations, affecting the O$_3$ formation.

513   These results highlight the significance of HCHO in the photochemical reactions

514   occurring in the coastal city during the co-occurring O$_3$ and PM$_{2.5}$ pollution

515   ~~period~~events.
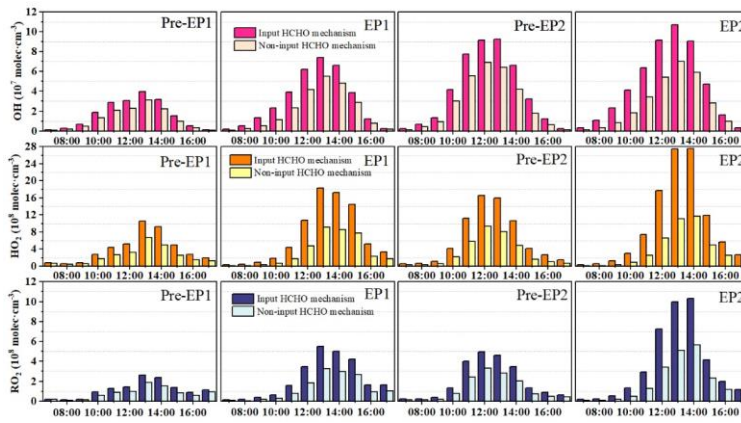
516

517   **Figure ~~9~~8. OH, HO$_2$, and RO$_2$ concentrations modeled by the OBM with or without the**
518   **HCHO mechanism**

519

520

521

Conclusions

523   A wintertime co-occurring O_3 and $PM_{2.5}$ pollution event was selected to investigate

524   the synergistic effects between $PM_{2.5}$ and O_3 in a coastal city in southeast China. The

525   results domonstrated a positive correlation between $PM_{2.5}$ and MDA8 O_3

526   concentrations during the whole periods, indicating the enhancement of atmospheric

527   oxidation capacity (AOC) during cold seasons. The result of positive matrix

528   factorization (PMF) analysis suggested that the contribution of secondary formation to

529    $PM_{2.5}$ increased during the pollution events, implying that the elevated AOC promoted

530   the oxidation of SO_2, NOx, and VOCs, leading to the formation of secondary inorganic

531   and organic components. We also ~~observed~~found the significant correlations ($R^2 =$

532   0.415–0.477) between HCHO, Fe, Mn, and sulfate concentrations, suggesting the

533   influence of catalyzed oxidation in the coastal city. Through OBM analysis, we

534   demonstrated that high concentrations of precursors (SO_2 and HCHO), high RH, and

535   moderately acidic pH conditions enhanced the heterogeneous formation of

536   hydroxymethanesulfonate (HMS). Meanwhile, we verified that the input HCHO

537   mechanism increased the concentrations of ROx and net O_3 production rates. Moreover,

538   the production rates of HO_2+NO and RO_2+NO were enhanced, indicating that HCHO

539   affected O_3 formation by controlling the efficiencies of radical propagation. This study

540   highlighted the influence of the HCHO mechanism on photochemical reactions and the

541   formation of HMS in~~co-occurring O_3 and~~ $PM_{2.5}$ ~~pollution~~ in coastal cities and was

542   beneficial for improving air quality and protecting public health.

543

Data Availability. The data set related to this work can be accessed via https://doi.org/10.5281/zenodo.7799302 (Hong, 2023). The details are also available upon request from the corresponding author (ywhong@iue.ac.cn).

547

548

Authorship Contribution Statement. ~~YW~~Youwei Hong designed and wrote the manuscript. Y~~iling~~L Lin ~~–~~and ~~L~~Dan Liao collected the data~~, and~~. ~~GJ~~Gaojie Chen and ~~Z~~Min Zhao contributed to the modeling analyses. ~~KR~~Keran Zhang, ~~XT~~Xiaoting Ji, ~~X~~Ke Xu~~,~~ and ~~W~~Yu Wu performed data analysis. Sung-Deuk Choi~~SD~~, ~~LK~~Likun Xue, ~~RL~~Ruilian Yu~~,~~ and ~~GR~~ Gongren Hu contributed to revising the manuscript. ~~JS~~Jinsheng Chen supported funding of observation and research~~es~~.

555

Competing interests. The authors declare that they have no conflict of interest.

557

Acknowledgement. The authors gratefully acknowledge Yanting Chen and Zhiqian Shao (Institute of Urban Environment, Chinese Academy of Sciences) for their guidance and assistance during the observation, and Lingling Xu, Mengren Li, and Xiaolong Fan (Institute of Urban Environment, Chinese Academy of Sciences) for the discussion of this paper. This research was supported by the Xiamen Atmospheric Environment Observation and Research Station of Fujian Province (Institute of Urban Environment, Chinese Academy of Sciences).

565

Financial support. This research was financially supported by the National Natural Science Foundation of China (42277091, U22A20578), the foreign cooperation project of Fujian Province (2020I0038), the Xiamen Youth Innovation Fund Project (3502Z20206094), the FJIRSM&IUE Joint Research Fund (RHZX-2019-006), and Center for Excellence in Regional Atmospheric Environment project (E0L1B20201).

References

Belis, C. A., Pikridas, M., Lucarelli, F., Petralia, E., Cavalli, F., Calzolai, G., Berico, M., and Sciare, J.: Source apportionment of fine PM by combining high time resolution organic and inorganic chemical composition datasets, Atmos. Environ.-X, 3, 10.1016/j.aeaoa.2019.100046, 2019.

Campbell, J. R., Battaglia, M., Dingilian, K., Cesler-Maloney, M., St Clair, J. M., Hanisco, T. F., Robinson, E., DeCarlo, P., Simpson, W., Nenes, A., Weber, R. J., and Mao, J.: Source and Chemistry of Hydroxymethanesulfonate (HMS) in Fairbanks, Alaska, Environ. Sci. Technol., 10.1021/acs.est.2c00410, 2022.

Chen, G., Liu, T., Ji, X., Xu, K., Hong, Y*., Xu, L., Li, M., Fan, X., Chen, Y., Yang, C., Lin, Z., Huang, W., and Chen, J.: Source Apportionment of VOCs and O_3 Production Sensitivity at Coastal and Inland Sites of Southeast China, Aerosol Air Qual. Res., 22, 220289, 10.4209/aaqr.220289, 2022.

Chow, W. S., Liao, K., Huang, X. H. H., Leung, K. F., Lau, A. K. H., and Yu, J. Z.: Measurement report: The 10-year trend of PM2.5 major components and source tracers from 2008 to 2017 in an urban site of Hong Kong, China, Atmos. Chem. Phys., 22, 11557-11577, 10.5194/acp-22-11557-2022, 2022.

Dixon, R. W. and Aasen, H.: Measurement of hydroxymethanesulfonate in atmospheric aerosols, Atmos. Environ., 33, 2023–2029, https://doi.org/10.1016/s1352-2310(98)00416-6, 1999.

Dovrou, E., Bates, K. H., Moch, J. M., Mickley, L. J., Jacob, D. J., and Keutsch, F. N.: Catalytic role of formaldehyde in particulate matter formation, P. Natl. Acad. Sci. USA, 119, e2113265119, 10.1073/pnas.2113265119, 2022.

Feng, T., Zhao, S., Zhang, X., Wang, Q., Liu, L., Li, G., and Tie, X.: Increasing wintertime ozone levels and secondary aerosol formation in the Guanzhong basin, central China, Sci. Total Environ., 745, 10.1016/j.scitotenv.2020.140961, 2020.

Gen, M., Zhang, R., Huang, D. D., Li, Y., and Chan, C. K.: Heterogeneous SO2 Oxidation in Sulfate

Formation by Photolysis of Particulate Nitrate, Environ. Sci. Technol. Letters, 6, 86-91, 10.1021/acs.estlett.8b00681, 2019.

Hong, Y., Xu, X., Liao, D., Zheng, R., Ji, X., Chen, Y., Xu, L., Li, M., Wang, H., Xiao, H., Choi, S.-D., and Chen, J.: Source apportionment of PM2.5 and sulfate formation during the COVID-19 lockdown in a coastal city of southeast China, Environ. Pollut., 286, 117577, https://doi.org/10.1016/j.envpol.2021.117577, 2021.

Hong, Y., Xu, X., Liao, D., Liu, T., Ji, X., Xu, K., Liao, C., Wang, T., Lin, C., and Chen, J.: Measurement report: Effects of anthropogenic emissions and environmental factors on the formation of biogenic secondary organic aerosol (BSOA) in a coastal city of southeastern China, Atmos. Chem. Phys., 22, 7827-7841, 10.5194/acp-22-7827-2022, 2022.

Hong, youwei. (2023). Dataset for ACP by Hong et al., 2023 [Data set]. Zenodo. 584 https://doi.org/10.5281/zenodo. 7799302.

Hu, B., Duan, J., Hong, Y., Xu, L., Li, M., Bian, Y., Qin, M., Fang, W., Xie, P., and Chen, J.: Exploration of the atmospheric chemistry of nitrous acid in a coastal city of southeastern China: results from measurements across four seasons, Atmos. Chem. Phys., 22, 371-393, 10.5194/acp-22-371-2022, 2022.

Ivatt, P. D., Evans, M. J., and Lewis, A. C.: Suppression of surface ozone by an aerosol-inhibited photochemical ozone regime, Nat. Geosci., 10.1038/s41561-022-00972-9, 2022.

Ji, X., Xu, K., Liao, D., Chen, G., Liu, T., Hong, Y. *, Dong, S., Choi, S.-D., and Chen, J.*: Spatial-temporal Characteristics and Source Apportionment of Ambient VOCs in Southeast Mountain Area of China, Aerosol Air Qual. Res., 22, 220016, 2022.

Jia, C., Tong, S., Zhang, X., Li, F., Zhang, W., Li, W., Wang, Z., Zhang, G., Tang, G., Liu, Z., and Ge, M.: Atmospheric oxidizing capacity in autumn Beijing: Analysis of the O_3 and $PM_{2.5}$ episodes based on observation-based model, J Environ. Sci., 124, 557-569, https://doi.org/10.1016/j.jes.2021.11.020, 2023.

Jiang, Y., Wang, S., Xing, J., Zhao, B., Li, S., Chang, X., Zhang, S., and Dong, Z.: Ambient fine particulate matter and ozone pollution in China: Synergy in anthropogenic emissions and atmospheric processes, Environ. Res. Lett., 2022.

Kalashnikov, D. A., Schnell, J. L., Abatzoglou, J. T., Swain, D. L., and Singh, D.: Increasing co-

627   occurrence of fine particulate matter and ground-level ozone extremes in the western United States,

628   Sci. Adv., 8, 10.1126/sciadv.abi9386, 2022.

629   Li, Zhanqing, Guo, Jianping, Ding, Aijun, Liao, Hong, Liu, and Jianjun: Aerosol and boundary-layer

630   interactions and impact on air quality, Nat. Sci. Rev., 2017.

631   Li, J., Zhang, Y.-L., Cao, F., Zhang, W., Fan, M., Lee, X., and Michalski, G.: Stable Sulfur Isotopes

632   Revealed a Major Role of Transition-Metal Ion-Catalyzed SO2 Oxidation in Haze Episodes,

633   Environ. Sci. Technol., 54, 2626-2634, 10.1021/acs.est.9b07150, 2020.

634   Li, K., Jacob, D. J., Liao, H., Shen, L., Zhang, Q., and Bates, K. H.: Anthropogenic drivers of 2013-2017

635   trends in summer surface ozone in China, P. Natl. Acad. Sci. USA of the United States of America,

636   116, 422-427, 10.1073/pnas.1812168116, 2019a.

637   Li, K., Jacob, D. J., Liao, H., Zhu, J., Shah, V., Shen, L., Bates, K. H., Zhang, Q., and Zhai, S.: A two-

638   pollutant strategy for improving ozone and particulate air quality in China, Nat. Geosci., 12, 906-+,

639   10.1038/s41561-019-0464-x, 2019b.

640   Li, Y., Zhang, Z., and Xing, Y.: Long-Term Change Analysis of PM2.5 and Ozone Pollution in China's

641   Most Polluted Region during 2015-2020, Atmosphere, 13, 10.3390/atmos13010104, 2022.

642   Li, Z., Xue, L., Yang, X., Zha, Q., Tham, Y. J., Yan, C., Louie, P. K. K., Luk, C. W. Y., Wang, T., and

643   Wang, W.: Oxidizing capacity of the rural atmosphere in Hong Kong, Southern China, Sci. Total

644   Environ., 612, 1114-1122, https://doi.org/10.1016/j.scitotenv.2017.08.310, 2018.

645   Liu, T., Clegg, S. L., and Abbatt, J. P. D.: Fast oxidation of sulfur dioxide by hydrogen peroxide in

646   deliquesced aerosol particles, P. Natl. Acad. Sci. USA, 117, 1354-1359, 10.1073/pnas.1916401117,

647   2020a.

648   Liu, T., Hu, B., Yang, Y., Li, M., Hong, Y., Xu, X., Xu, L., Chen, N., Chen, Y., Xiao, H., and Chen, J.:

649   Characteristics and source apportionment of PM2.5 on an island in Southeast China: Impact of sea-

650   salt and monsoon, Atmos. Res., 235, 10.1016/j.atmosres.2019.104786, 2020.

651   Liu, T., Hong, Y., Li, M., Xu, L., Chen, J., Bian, Y., Yang, C., Dan, Y., Zhang, Y., Xue, L., Zhao, M.,

652   Huang, Z., and Wang, H.: Atmospheric oxidation capacity and ozone pollution mechanism in a

653   coastal city of southeastern China: analysis of a typical photochemical episode by an observation-

654   based model, Atmos. Chem. Phys., 22, 2173-2190, 10.5194/acp-22-2173-2022, 2022a.

655   Liu, T., Lin, Y., Chen, J., Chen, G., Yang, C., Xu, L., Li, M., Fan, X., Zhang, F., and Hong, Y.: Pollution

656   mechanisms and photochemical effects of atmospheric HCHO in a coastal city of southeast China,

657   Sci. Total Environ., 160210, https://doi.org/10.1016/j.scitotenv.2022.160210, 2022b.

658   Lou, S., Liao, H., and Zhu, B.: Impacts of aerosols on surface-layer ozone concentrations in China

659   through heterogeneous reactions and changes in photolysis rates, Atmos. Environ., 85, 123-138,

660   https://doi.org/10.1016/j.atmosenv.2013.12.004, 2014.

661   Lu, K., Guo, S., Tan, Z., Wang, H., Shang, D., Liu, Y., Li, X., Wu, Z., Hu, M., and Zhang, Y.: Exploring

662   atmospheric free-radical chemistry in China:the self-cleansing capacity and the formation of

663   secondary air pollution, Nat. Sci. Rev., 6, 579-594, 2019.

664   Ma, T., Furutani, H., Duan, F., Kimoto, T., Jiang, J., Zhang, Q., Xu, X., Wang, Y., Gao, J., Geng, G., Li,

665   M., Song, S., Ma, Y., Che, F., Wang, J., Zhu, L., Huang, T., Toyoda, M., and He, K.: Contribution

666   of hydroxymethanesulfonate (HMS) to severe winter haze in the North China Plain, Atmos. Chem.

667   Phys., 20, 5887–5897, https://doi.org/10.5194/acp-20-5887-2020, 2020.

668   Mitsuishi, K.; Iwasaki, M.; Takeuchi, M.; Okochi, H.; Kato, S.; Ohira, S. I.; Toda, K., Diurnal

669   Variations in Partitioning of Atmospheric Glyoxal and Methylglyoxal between Gas and

670   Particles at the Ground Level and in the Free Troposphere. Acs Earth and Space Chemistry

671   2018, 2, (9), 915-924.

672   Moch, J. M., Dovrou, E., Mickley, L. J., Keutsch, F. N., Cheng, Y., Jacob, D. J., Jiang, J. K., Li, M.,

673   Munger, J. W., Qiao, X. H., Zhang, Q.: Contribution of Hydroxymethane Sulfonate to Ambient

674   Particulate Matter: A Potential Explanation for High Particulate Sulfur During Severe Winter

675   Haze in Beijing, Geophysical Research Letters, 45, (21), 11969-11979, 2018.

676   Moch, J. M.; Dovrou E., Mickley L. J., Keutsch F. N., Liu Z., Wang Y., et al. Global Importance of

677   Hydroxymethanesulfonate in Ambient Particulate Matter: Implications for Air Quality. J

678   Geophys. Res.-Atmospheres 2020, 125(18),1-14

679   Moch, J. M., Dovrou, E., Mickley, L. J., Keutsch, F. N., Liu, Z., Wang, Y., Dombek, T. L., Kuwata,

680   M., Budisulistiorini, S. H., Yang, L., Decesari, S., Paglione, M., Alexander, B., Shao, J.,

681   Munger, J. W., and Jacob, D. J.: Global Importance of Hydroxymethanesulfonate in Ambient

682   Particulate Matter: Implications for Air Quality, J Geophys. Res.-Atmospheres, 125,

683   10.1029/2020jd032706, 2020

684   Munger, J. W., Tiller, C., and Hoffmann, M. R.: Identification of hydroxymethanesulfonate in fog

water, Science, 231, 247–249, https://doi.org/10.1126/science.231.4735.247, 1986.

Polissar, A. V., Hopke, P. K., and Paatero, P.: Atmospheric aerosol over Alaska - 2. Elemental composition and sources, J Geophys. Res.-Atmospheres, 103, 19045-19057, 10.1029/98jd01212, 1998.

Qin, M., Hu, A., Mao, J., Li, X., Sheng, L., Sun, J., Li, J., Wang, X., Zhang, Y., and Hu, J.: PM2.5 and O3 relationships affected by the atmospheric oxidizing capacity in the Yangtze River Delta, China, Sci. Total Environ., 810, 152268, https://doi.org/10.1016/j.scitotenv.2021.152268, 2022.

Qin, Y., Li, J., Gong, K., Wu, Z., Chen, M., Qin, M., Huang, L., and Hu, J.: Double high pollution events in the Yangtze River Delta from 2015 to 2019: Characteristics, trends, and meteorological situations, Sci. Total Environ., 792, 10.1016/j.scitotenv.2021.148349, 2021.

Qu, Y., Wang, T., Yuan, C., Wu, H., Gao, L., Huang, C., Li, Y., Li, M., and Xie, M.: The underlying mechanisms of PM2.5 and O3 synergistic pollution in East China: Photochemical and heterogeneous interactions, Sci. Total Environ., 873, 162434, https://doi.org/10.1016/j.scitotenv.2023.162434, 2023.

Rienda, I. C., and Alves, C. A.: Road dust resuspension: A review, Atmos. Res., 261, 10.1016/j.atmosres.2021.105740, 2021.

Schwartz, S. E. In Mass-Transport Considerations Pertinent to Aqueous Phase Reactions of Gases in Liquid-Water Clouds, Chemistry of Multiphase Atmospheric Systems, Jaeschke, W., Ed. Springer Berlin Heidelberg: Berlin, Heidelberg, 1986; pp 415-471.

Shao, M., Wang, W., Yuan, B., Parrish, D. D., Li, X., Lu, K., Wu, L., Wang, X., Mo, Z., Yang, S., Peng, Y., Kuang, Y., Chen, W., Hu, M., Zeng, L., Su, H., Cheng, Y., Zheng, J., and Zhang, Y.: Quantifying the role of PM2.5 dropping in variations of ground-level ozone: Inter-comparison between Beijing and Los Angeles, Sci. Total Environ., 788, 147712, https://doi.org/10.1016/j.scitotenv.2021.147712, 2021.

Shao, M., Yang, J., Wang, J., Chen, P., Liu, B., and Dai, Q.: Co-Occurrence of Surface O3, PM2.5 Pollution, and Tropical Cyclones in China, J Geophys. Res.Atmospheres, 127, e2021JD036310, https://doi.org/10.1029/2021JD036310, 2022.

Song, H., Lu, K., Dong, H., Tan, Z., Chen, S., Zeng, L., and Zhang, Y.: Reduced Aerosol Uptake of Hydroperoxyl Radical May Increase the Sensitivity of Ozone Production to Volatile Organic Compounds, Environ. Sci. Technol. Lett., 9, 22-29, 10.1021/acs.estlett.1c00893, 2022.

714 Song, S., Ma, T., Zhang, Y., Shen, L., Liu, P., Li, K., Zhai, S., Zheng, H., Gao, M., Moch, J. M., Duan,
715   F., He, K., and McElroy, M. B.: Global modeling of heterogeneous hydroxymethanesulfonate
716   chemistry, Atmos. Chem. Phys., 21, 457–481, https://doi.org/10.5194/acp-21-457-2021, 2021.

717 Vohra, K., Marais, E. A., Bloss, W. J., Schwartz, J., Mickley, L. J., Van Damme, M., Clarisse, L., and
718   Coheur, P.-F.: Rapid rise in premature mortality due to anthropogenic air pollution in fast-growing
719   tropical cities from 2005 to 2018, Sci. Adv., 8, eabm4435-eabm4435, 10.1126/sciadv.abm4435,
720   2022.

721 Wang, S., Zhao, Y., Chan, A. W. H., Yao, M., Chen, Z., and Abbatt, J. P. D.: Organic Peroxides in Aerosol:
722   Key Reactive Intermediates for Multiphase Processes in the Atmosphere, Chem. Rev.,
723   10.1021/acs.chemrev.2c00430, 2023.

724 Wang, W., Liu, M., Wang, T., Song, Y., Zhou, L., Cao, J., Hu, J., Tang, G., Chen, Z., Li, Z., Xu, Z., Peng,
725   C., Lian, C., Chen, Y., Pan, Y., Zhang, Y., Sun, Y., Li, W., Zhu, T., Tian, H., and Ge, M.: Sulfate
726   formation is dominated by manganese-catalyzed oxidation of SO2 on aerosol surfaces during haze
727   events, Nat. Commun., 12, 10.1038/s41467-021-22091-6, 2021.

728 Watson, J. G., Chow, J. C., and Houck, J. E.: PM2.5 chemical source profiles for vehicle exhaust,
729   vegetative burning, geological material, and coal burning in Northwestern Colorado during 1995,
730   Chemo., 43, 1141-1151, 10.1016/s0045-6535(00)00171-5, 2001.

731 World Health Organization. WHO global air quality guidelines: particulate matter (PM2.5 and PM10),
732   ozone, nitrogen dioxide, sulfur dioxide and carbon monoxide. 2021 (2021-12-21). ISBN 978-92-4-
733   003422-8

734 Wu, X., Xu, L. L., Hong, Y. W., Chen, J. F., Qiu, Y. Q., Hu, B. Y., Hong, Z. Y., Zhang, Y. R., Liu, T. T.,
735   Chen, Y. T., Bian, Y. H., Zhao, G. Q., Chen, J. S., and Li, M. R.: The air pollution governed by
736   subtropical high in a coastal city in Southeast China: Formation processes and influencing
737   mechanisms, Sci. Total Environ., 692, 1135-1145, 10.1016/j.scitotenv.2019.07.341, 2019.

738 Wu, X., Li, M., Chen, J., Wang, H., Xu, L., Hong, Y., Zhao, G., Hu, B., Zhang, Y., Dan, Y., and Yu, S.:
739   The characteristics of air pollution induced by the quasi-stationary front: Formation processes and
740   influencing factors, Sci. Total Environ., 707, 10.1016/j.scitotenv.2019.136194, 2020.

741 Wu, Y., Huo, J., Yang, G., Wang, Y., Wang, L., Wu, S., Yao, L., Fu, Q., and Wang, L.: Measurement report:
742   Production and loss of atmospheric formaldehyde at a suburban site of Shanghai in summertime,

Atmos. Chem. Phys., 23, 2997-3014, 10.5194/acp-23-2997-2023, 2023.

Xiao, Q., Geng, G., Xue, T., Liu, S., Cai, C., He, K., and Zhang, Q.: Tracking PM2.5 and O-3 Pollution and the Related Health Burden in China 2013-2020, Environ. Sci. Technol., 56, 6922-6932, 10.1021/acs.est.1c04548, 2022.

Xu, R., Li, X., Dong, H., Lv, D., Kim, N., Yang, S., Wang, W., Chen, J., Shao, M., Lu, S., Wu, Z., Chen, S., Guo, S., Hu, M., Liu, Y., Zeng, L., and Zhang, Y.: Field observations and quantifications of atmospheric formaldehyde partitioning in gaseous and particulate phases, Sci. Total Environ., 808, 10.1016/j.scitotenv.2021.152122, 2022.

Xue, L., Gu, R., Wang, T., Wang, X., Saunders, S., Blake, D., Louie, P. K. K., Luk, C. W. Y., Simpson, I., Xu, Z., Wang, Z., Gao, Y., Lee, S., Mellouki, A., and Wang, W.: Oxidative capacity and radical chemistry in the polluted atmosphere of Hong Kong and Pearl River Delta region: analysis of a severe photochemical smog episode, Atmos. Chem. Phys., 16, 9891-9903, 10.5194/acp-16-9891-2016, 2016.

Zhang, K., Duan, Y., Huo, J., Huang, L., Wang, Y., Fu, Q., Wang, Y., and Li, L.: Formation mechanism of HCHO pollution in the suburban Yangtze River Delta region, China: A box model study and policy implementations, Atmos. Environ., 267, 118755, https://doi.org/10.1016/j.atmosenv.2021.118755, 2021.

Zhang, N., Guan, Y., Jiang, Y., Zhang, X., Ding, D., and Wang, S.: Regional demarcation of synergistic control for PM2.5 and ozone pollution in China based on long-term and massive data mining, Sci. Total Environ., 155975, https://doi.org/10.1016/j.scitotenv.2022.155975, 2022.

Zhao, D., Liu, G., Xin, J., Quan, J., Wang, Y., Wang, X., Dai, L., Gao, W., Tang, G., Hu, B., Ma, Y., Wu, X., Wang, L., Liu, Z., and Wu, F.: Haze pollution under a high atmospheric oxidization capacity in summer in Beijing: insights into formation mechanism of atmospheric physicochemical processes, Atmos. Chem. Phys., 20, 4575-4592, 10.5194/acp-20-4575-2020, 2020.

Zong, L., Yang, Y., Gao, M., Wang, H., Wang, P., Zhang, H., Wang, L., Ning, G., Liu, C., Li, Y., and Gao, Z.: Large-scale synoptic drivers of co-occurring summertime ozone and PM2.5 pollution in eastern China, Atmos. Chem. Phys., 21, 9105-9124, 10.5194/acp-21-9105-2021, 2021.